

# Electrodeposition of Ni-Fe-Co-Graphene Composite Coatings and Their Electrocatalytic Activity for Hydrogen Evolution Reaction

Shuliang Wang<sup>1,2,\*</sup>, Wanting Li<sup>1</sup>, Haisen Qin<sup>1</sup>, Li Liu<sup>1</sup>, Yuyao Chen<sup>1</sup>, Dinghan Xiang<sup>2</sup>

<sup>1</sup> School of Materials Science and Engineering, Southwest Petroleum University, Chengdu 610500, P.R. China

<sup>2</sup> Guangxi Key Laboratory of Information Materials, Guilin University of Electronic Technology, Guilin 541004, P.R. China

\*E-mail: [wsliang1465@126.com](mailto:wsliang1465@126.com)

*Received:* 30 September 2018 / *Accepted:* 13 November 2018 / *Published:* 30 November 2018

---

In this study, composite coatings of Ni-Fe-Co-graphene were successfully produced via electrodeposition on a steel substrate from sulfate acidic bath under different conditions. Findings showed that the incorporation of graphene could improve the electrocatalytic activity of the coatings for hydrogen evolution reaction (HER) in an alkaline environment. As indicated by linear sweep voltammetry and electrochemical impedance spectroscopy measurements in 6 M KOH, the best coating (graphene concentration of 0.2 g L<sup>-1</sup>) presented a low overpotential (169 mV at 10 mA cm<sup>-2</sup>), high exchange current density (272.3 μA cm<sup>-2</sup>), and large electrochemical surface area (686.5 cm<sup>2</sup>). Tafel slope analysis showed that HER occurred on the composite coatings via the Volmer–Heyrovsky mechanism. Relevant conclusions were validated by scanning electron microscopy, energy dispersive spectrometer, X-ray diffraction, and electrochemical workstation.

---

**Keywords:** Electrodeposition composite coating; transition metal; electro-catalytic activity; hydrogen evolution reaction; alkaline solution

## 1. INTRODUCTION

With the energy crisis and environmental pollution, the development of new energy and renewable energy has been attracting considerable attention from various countries. Meanwhile, hydrogen is clean, efficient, and can be stored and transported and is thus regarded as an ideal energy carrier [1, 2]. In various hydrogen production technologies, the use of renewable energy generated by electric energy into hydrogen is promising [3]. Water electrolysis exhibits high purity, high electrolytic efficiency, lack of pollution, and other advantages; however, the problem of high energy consumption

in the electrolysis process remains unsolved. Platinum electrodes have many excellent properties in electrocatalysis, but they are expensive [4]. Molybdenum and tungsten electrodes show good activity for hydrogen evolution reaction (HER), but their low natural abundance limits their applications for industrial production [5, 6]. Therefore, developing an excellent electrode material with superior electrocatalytic activity, low energy consumption, stable electrochemical performance, and low cost for HER has become a general consensus [7].

Energy consumption could be reduced by the lowering of the cathode overpotential (electronic factor) and increase in the active surface area (geometrical factor) [8]. A low overpotential for HER is mainly influenced by the intrinsic property of materials. From electrocatalytic theory, the adsorption bond of a hydrogen atom is mainly formed by the electron of a hydrogen atom with an unpaired d-electron of the metal [9]. Late transition metals, such as Mn, Fe, Co, Ni, and Cu, have numerous unpaired d-electrons and unfilled d-orbitals, which could easily form an adsorption bond with the adsorbate (H atom). Among these transition metals, Ni is promising for use in HER because of its high theoretical catalytic activity, sufficient corrosion resistance, and cost-effectiveness. To maximize the intrinsic activity of Ni for HER, other transition metals, such as Fe and Co, are usually incorporated [10, 11]. Given the synergistic interaction between transition metals, such metals could bring about changes to their bonding strength that would increase intermetallic stability. The stability maximum usually coincides with optimal d-electrons for the maximal activity in HER [12]. A previous study reported that alloy electrodes, such as Ni-Cu [13], Ni-Fe [14], and Ni-Co-P [15, 16], showed good electrocatalytic properties in HER.

Enlarging the active surface area of the electrode is another means of improving electrocatalytic activity and reducing energy consumption. For enlarging the electrochemical surface area of the alloy electrode, nanoparticles such as TiO<sub>2</sub> [17] and carbon nanopowder [18-20] are used as second phase particles. Graphene, as a wonder material of carbon nanomaterials, has attracted extensive attention and research due to its high migration rate of the charge (15000 cm<sup>2</sup> V<sup>-1</sup> s<sup>-1</sup> at room temperature) [21] and large specific surface area (0.77 mg m<sup>-2</sup>) [22]. The graphene used as support in the electrode can enhance electron transport and expand the BET surface area, which is beneficial for improving the electrocatalytic properties of electrode materials. Hence, the remarkable characteristics of graphene allow for the development of an excellent composite electrode via graphene in combination with transition metals. For example, a study proposed that the electrocatalytic activity for the hydrogen evolution of Ni-Co alloy was considerably improved by the covering of an ultrathin graphene layer with an acidic solution [23]. The electrocatalytic activities of Fe-Ni-graphene and Co-Ni-graphene composite electrodes in alkaline solutions were three and four times those of Fe-Ni and Co-Ni electrodes, respectively [24, 25].

In this work, different Ni-Fe-Co-graphene composite coatings were prepared under various graphene concentrations (0.05 g L<sup>-1</sup> to 0.8 g L<sup>-1</sup>) by direct current electrodeposition. The surface morphology, chemical composition, and phase structure of the coatings were investigated by scanning electron microscopy (SEM), energy dispersive spectrometer (EDS), and X-ray diffraction (XRD). Linear sweep voltammetry (LSV), chronopotentiometry tests, and electrochemical impedance spectroscopy (EIS) were used for evaluating the electrocatalytic activity for HER in an alkaline solution. In addition, the apparent activation energy of the best Ni-Fe-Co-graphene composite coating was also studied and discussed.

## 2. EXPERIMENTAL

### 2.1. Materials and methods

Plate specimens measuring 10 mm × 10 mm × 2 mm were extracted from Q235 steel and then ground using silicon carbide papers up to 2000 grit. Prior to electrodeposition, the specimens were degreased by acetone, cleaned by deionized water, rinsed by alcohol, and then immediately dried by a blow drier. The Ni-Fe-Co-graphene coatings were electrodeposited in an acid sulfate bath. The composition of the electrolyte is listed in Table 1. The pH value of the bath was adjusted to 3.8 via NaOH and HCl, and then, the bath was agitated ultrasonically for 12 h before the deposition. The processed Q235 steel was used as cathode, and a pure Ni strip with equal exposed surface area was used as anode. The cathode and anode were placed parallel to each other at 3 cm distance during plating. The electrochemical potentiostat was used for deposition by chronopotentiometry. All deposition conditions with containing time of 1800 s, current density of 60 mA cm<sup>-2</sup>, and temperature of 333 K were deemed suitable for comparisons. Magnetic stirring was also used during deposition.

For correlating the electrocatalytic property of the Ni-Fe-Co-graphene composite coatings with the graphene concentration added into the electrolyte, in total five concentrations at the concentrations of 0.05, 0.1, 0.2, 0.4, and 0.8 g L<sup>-1</sup> were employed for electrodeposition.

**Table 1.** Electrolyte composition for deposition of Ni-Fe-Co-graphene composite coatings

Composition	Concentration (g L <sup>-1</sup> )	Composition	Concentration (g L <sup>-1</sup> )
NiSO <sub>4</sub> ·6H <sub>2</sub> O	100	NaCl	20
NiCl·6H <sub>2</sub> O	15	H <sub>3</sub> BO <sub>3</sub>	25
CoSO <sub>4</sub> ·7H <sub>2</sub> O	8	Ascorbic acid	8
FeSO <sub>4</sub> ·7H <sub>2</sub> O	12	Trisodium citrate	25
Saccharin sodium salt	8	Sodium dodecyl sulfate	1

### 2.2. Characterization

The surface morphology and the elemental composition of the coatings were characterized by SEM and EDS (ZEISS EV0 MA15, Germany). The SEM measurements were performed at an accelerating voltage of 20 kV. The phase structures were analyzed using XRD (DX-2700X, China) with Cu K $\alpha$  radiation ( $\lambda=0.15418$  nm). The XRD was operated at a tube voltage of 40 kV, tube current of 60 mA, and scanning rate of 2° min<sup>-1</sup>.

Electrocatalytic studies of HER on the synthesized coatings were accomplished by LSV, chronopotentiometry, and EIS. All of the electrochemical tests were performed via an electrochemical workstation (Autolab Model PGSTAT302N, Netherlands) in 6 M KOH solution at room temperature unless otherwise specified. LSV curves were obtained in a potential range from -0.8 V to -1.8 V (vs. saturated calomel electrode [SCE]) with a scanning rate of 2 mV s<sup>-1</sup>. Chronopotentiometry measurements

were conducted at a constant current density of  $100 \text{ mA cm}^{-2}$  for 30000 s. EIS measurements were operated after the LSV curves were obtained. The measurements were performed in the frequency range of 100 KHz to 0.01 Hz, with an application of 5 mV amplitude sinusoidal voltage as disturbance signal.

In this system, the electrochemical measurements were put into effect through using a standard three-electrode electrochemical cell. A platinum electrode was used as the counter electrode, an SCE was used as the reference electrode, and a prepared coating was used as the test electrode. All the potentials of this work were referenced to a reversible hydrogen electrode (RHE):  $E (\text{vs. RHE}) = E (\text{vs. SCE}) + 0.244 + (0.059 \text{ V}) \text{ pH}$ . All experiments were performed when the electrochemical system was in a steady state.

### 3. RESULTS AND DISCUSSION

#### 3.1. Morphology and structure analyses

SEM and EDS analyses. SEM observations on the surface of Ni-Fe-Co alloy and Ni-Fe-Co-graphene composite coatings under different graphene concentration are shown in Fig. 1. Results showed that the addition of graphene in various concentrations into the electrolyte noticeably influenced the surface of the coatings. As shown in Fig. 1a, the flat surface of the Ni-Fe-Co alloy was stacked by even spherical particles. When the graphene concentration increased from  $0.05 \text{ g L}^{-1}$  to  $0.2 \text{ g L}^{-1}$  in the electrolyte, pellets of different sizes were piled up on the surface of Ni-Fe-Co-graphene coating, and smaller particles were formed on the local surface of large particles (Fig. 1b, 1c, and 1d). The spherical particles deposited on the surface of the Ni-Fe-Co-graphene composite coating under the graphene concentration of  $0.2 \text{ g L}^{-1}$  were the densest and most even among all the coatings, suggesting that this coating had the largest surface area (Fig. 1d). However, when the graphene concentration further increased from  $0.4 \text{ g L}^{-1}$  to  $0.8 \text{ g L}^{-1}$  in the electrolyte, a larger size and fewer number of particles were observed on the surface of the Ni-Fe-Co-graphene composite coating (Fig. 1e and 1f). Compared with the surface morphology under the graphene concentration of  $0.2 \text{ g L}^{-1}$ , the rough surface area with higher graphene concentration was smaller. Given graphene's prominent electrical conductivity and very high specific surface area of  $2276 \text{ m}^2 \text{ g}^{-1}$ , it was easily adsorbed in the cathodic coating surface. Therefore, graphene provided more active growth sites for metal atoms and promoted the co-deposition of transition metals from the electrolyte. Nevertheless, superfluous graphene did not easily disperse in the electrolyte on account of its serious aggregation, and the rough surface of Ni-Fe-Co-graphene composite coatings decreased noticeably. Table 2 shows the chemical composition of Ni-Fe-Co alloy and Ni-Fe-Co-graphene composite coatings produced under different graphene concentrations. The Fe and Co content of the coating under the graphene concentration of  $0.2 \text{ g L}^{-1}$  was the lowest among all the coatings, but its Ni content was the highest. This result was likely because  $\text{Ni}^{2+}$  is more easily absorbed on graphene platelets in comparison with  $\text{Fe}^{2+}$  and  $\text{Co}^{2+}$  during the deposition process. This situation was observed in other studies as well [26].

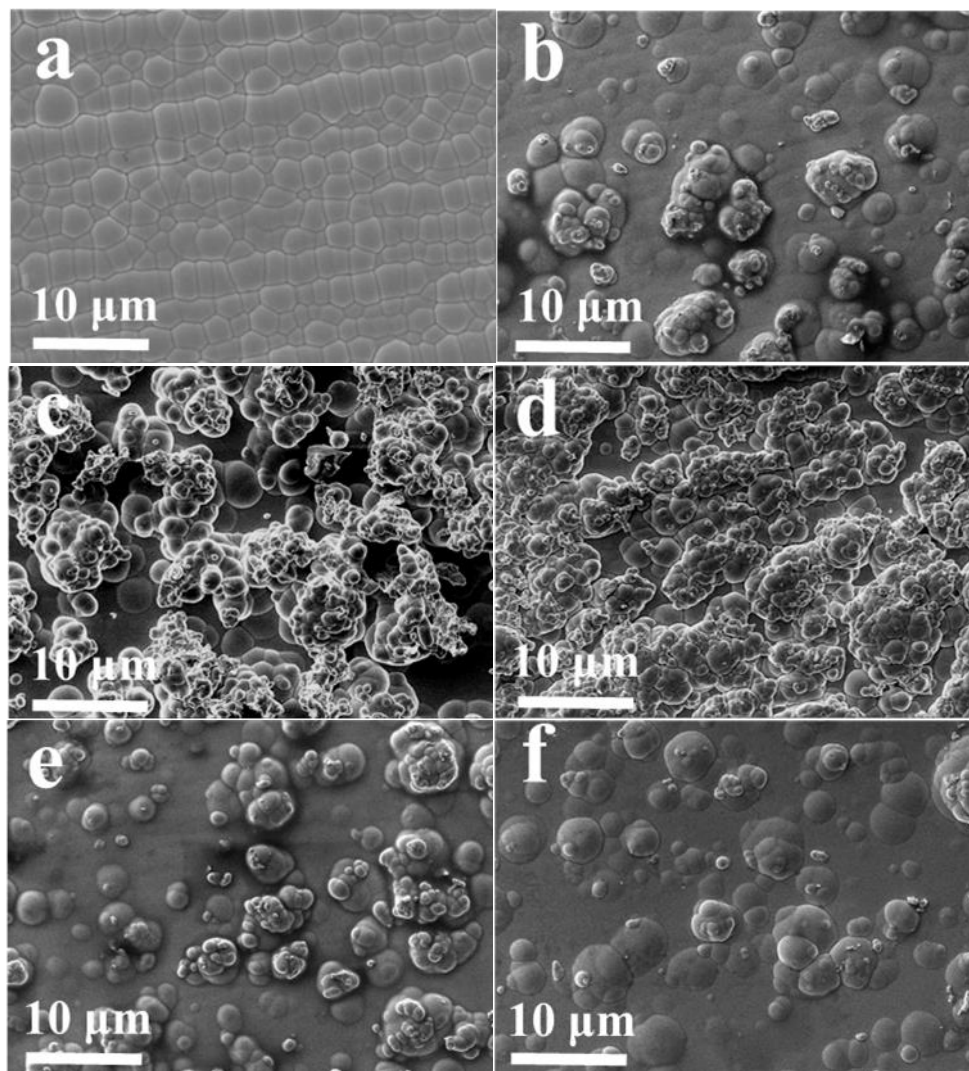


**Figure 1.** SEM images of (a) Ni-Fe-Co alloy and Ni-Fe-Co-graphene composite coatings deposited under different graphene concentrations of (b)  $0.05 \text{ g L}^{-1}$ , (c)  $0.1 \text{ g L}^{-1}$ , (d)  $0.2 \text{ g L}^{-1}$ , (e)  $0.4 \text{ g L}^{-1}$ , and (f)  $0.8 \text{ g L}^{-1}$ .

**Table 2.** Content of chemical element of Ni-Fe-Co alloy and Ni-Fe-Co-graphene composite coatings deposited under different graphene concentrations.

Concentration of graphene ( $\text{g L}^{-1}$ )	Fe (wt. %)	Co (wt. %)	Ni (wt. %)
–	34	24.14	41.86
0.05	33.85	23.91	42.24
0.1	32.56	25.30	42.14
0.2	30.48	25.05	44.47
0.4	32.72	24.64	42.64
0.8	34.91	23.56	41.53

The addition of graphene in electrolytes makes the coating surface rougher, and a rough surface exposes more active sites than does a flat surface in electrocatalysis [27]. However, superfluous graphene

seriously aggregated during electrodeposition; thus an appropriate concentration of graphene is essential for improving the electrocatalytic property of Ni-Fe-Co-graphene coatings.

XRD studies. The XRD patterns of the Ni-Fe-Co alloy and Ni-Fe-Co-graphene composite coatings under different graphene concentration are shown in Fig. 2a. Strong diffraction peaks were observed near  $44.28^\circ$  and  $51.47^\circ$  corresponding to the cubic structure of the Ni-Fe-Co alloy phase for all coatings. Previous studies reported that  $\text{Ni}_{1-x}\text{Fe}_x$  alloy at  $x < 58$  wt% is FCC phase, whereas  $\text{Ni}_{1-x}\text{Fe}_x$  alloy at  $x > 65$  wt% is only BCC phase [28]. Co is an iron group element for alloy composition [29, 30]. The total content of Fe and Co in the chemical composition for the Ni-Fe-Co alloy and the composite coatings under the graphene concentration of  $0.8 \text{ g L}^{-1}$  reached 58.14 wt% and 58.47 wt%, respectively, indicating that their phase structure may contain FCC with BCC. The composite coatings deposited under the graphene concentration of  $0.05 \text{ g L}^{-1}$  to  $0.4 \text{ g L}^{-1}$  corresponded to the FCC phase. Furthermore, no diffraction characteristic peak of graphene at around  $26.5^\circ$  was observed primarily due to the low content of graphene. The composite coating under the graphene concentration of  $0.2 \text{ g L}^{-1}$  showed a visibly broad full-width half-maximum and lower intensity in comparison, indicating that it had the poorest grain size. The average grain sizes of the coatings are shown in Fig. 3b according to the diffraction peaks by the Scherer formula (eq. 1) [31]:

$$D = \frac{0.89\lambda}{B\cos\theta} \quad (1)$$

where  $D$  represents crystallite size,  $\lambda$  represents the wavelength of incident X-ray,  $B$  represents the full-width at half-height of the symmetrical shape of the diffraction peak, and  $\theta$  represents the Bragg angle. The average grain size was 15.9 nm for the Ni-Fe-Co-graphene composite coating under the graphene concentration of  $0.2 \text{ g L}^{-1}$ , which was smaller than that of any other coating. This poor grain size could be potentially ascribed to the incorporation of graphene, which increases nucleation sites and inhibits the grain growth of Ni, Fe, and Co ions effectively.

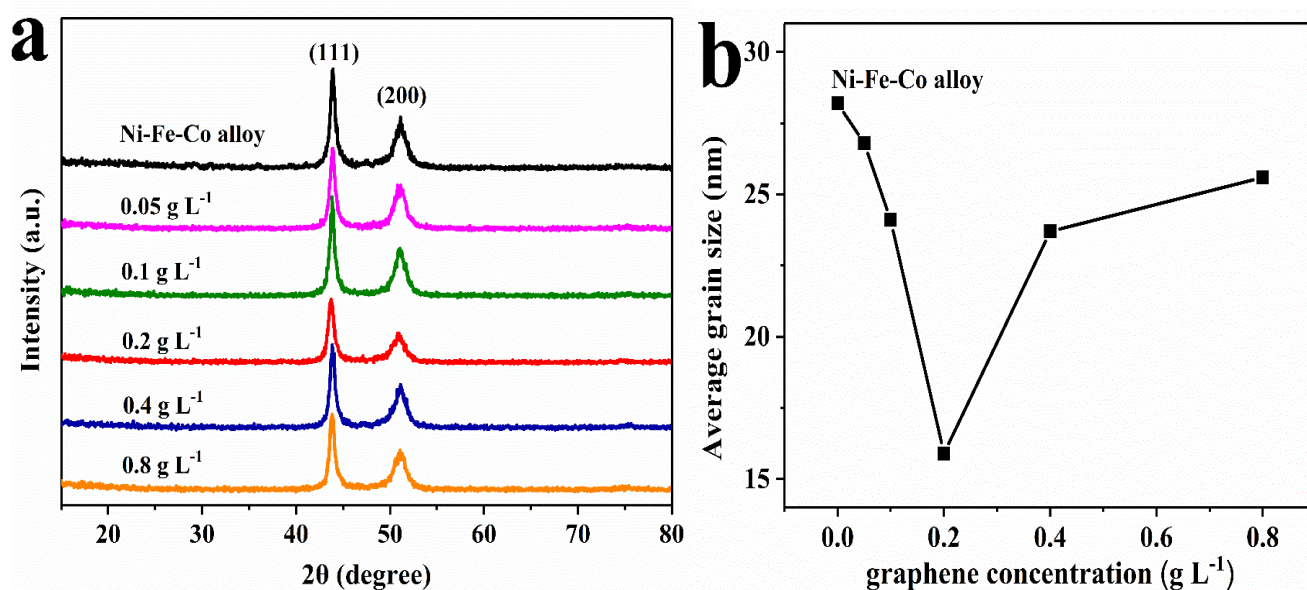


**Figure 2.** (a) XRD patterns and (b) average grain sizes of Ni-Fe-Co alloy and Ni-Fe-Co-graphene composite coatings deposited under different graphene concentrations.

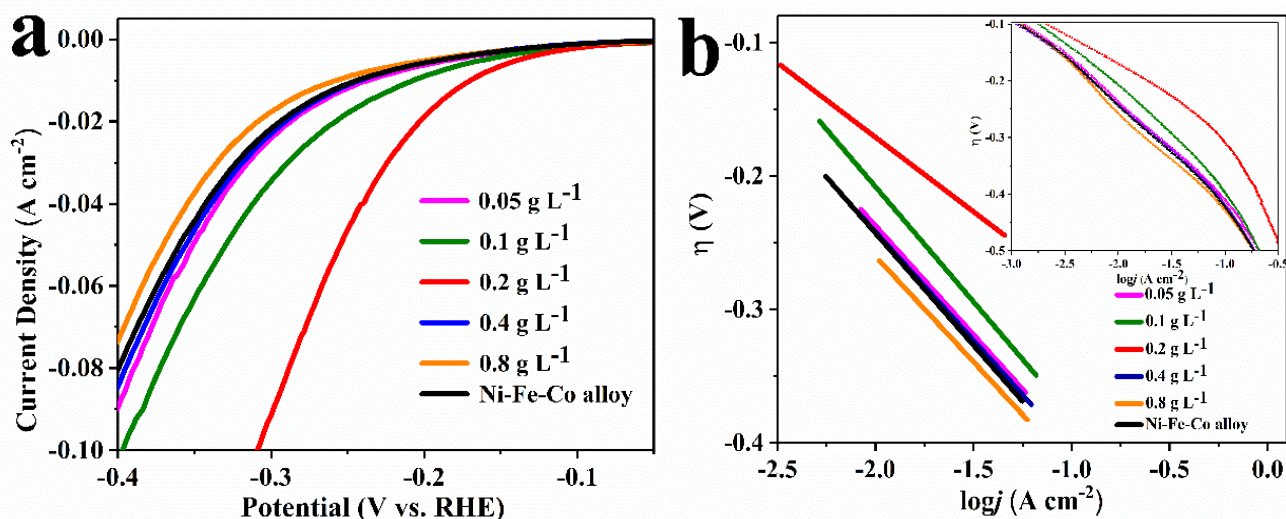
### 3.2. Electrochemical properties analyses

LSV curves and electrochemical stability observations. The cathodic LSV curves and Tafel slope are shown in Fig. 3a and 3b, respectively. The composite coating under the graphene concentration of  $0.2 \text{ g L}^{-1}$  showed the highest current density at the same potential, indicating an optimal electrocatalytic activity among all the coatings. The corresponding electrochemical-kinetic parameters followed the Tafel equations (eq. 2) [32]:

$$\eta = a + b \log j \quad (2)$$

where  $\eta$  is the overpotential,  $a$  is the Tafel intercept,  $b$  is the Tafel slope, and  $j$  is the current density. Apparent exchange current density values  $j_0$  are derived by extrapolation of Tafel plots to zero  $\eta$ . The kinetic parameters obtained by the fitting of the Tafel plots are listed in Table 3. The composite coating under the graphene concentration of  $0.2 \text{ g L}^{-1}$  showed the minimum overpotential (169 mV) at  $10 \text{ mA cm}^{-2}$ , which was noticeably lower than that of the Ni-Fe-Co alloy coating (243 mV), Ni-S-Fe (222 mV) [33], Ni-rGO (330 mV) [34], and so on. Additional details about the electrocatalysts for comparison are listed in Table 4. The calculated Tafel slope of the composite coating under the graphene concentration of  $0.2 \text{ g L}^{-1}$  was the smallest, indicating its faster HER electrocatalytic kinetics. Furthermore, the Tafel slopes of the coatings were close to the theoretical value of  $118 \text{ mV dec}^{-1}$ , illustrating that HER occurred on all coatings via the Volmer–Heyrovsky mechanism [35]. The exchange current density of the composite coating under the graphene concentration of  $0.2 \text{ g L}^{-1}$  ( $272.3 \text{ } \mu\text{A cm}^{-2}$ ) was approximately three times that of the Ni-Fe-Co alloy coating ( $83.8 \text{ } \mu\text{A cm}^{-2}$ ), indicating an enhanced intrinsic activity. These findings suggested that the introduction of graphene could evidently improve HER activity. The results were highly consistent with those from the literature [23-25, 36].

Furthermore, the electrochemical stabilities of the Ni-Fe-Co alloy and of the composite coating under the graphene concentration of  $0.2 \text{ g L}^{-1}$  for HER were obtained. As shown in Fig. 3c, the composite coating maintained a more stable potential at approximately 285 mV for a prolonged electrolysis test, which confirmed its remarkable stability and durability for HER. Moreover, the composite coating presented a lower overpotential than did the Ni-Fe-Co alloy, which was in accordance with the Tafel analysis results.



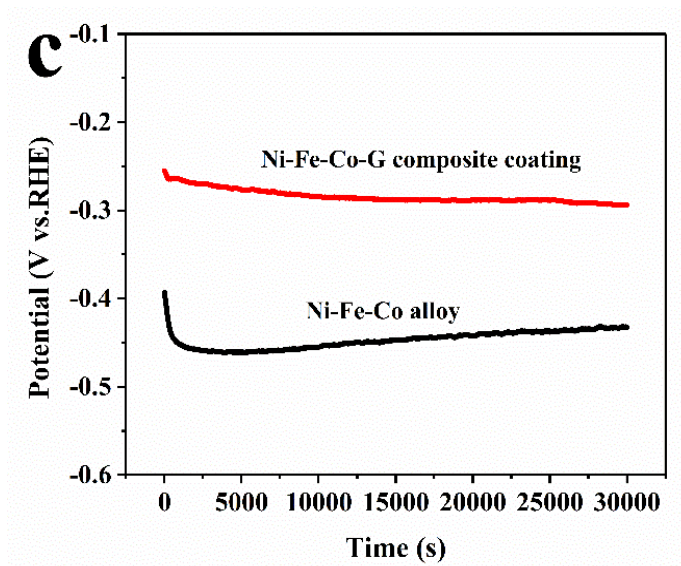


**Figure 3.** (a) LSV curves, (b) Tafel slopes and, (c) chronopotentiometry tests of Ni-Fe-Co alloy and Ni-Fe-Co-graphene composite coatings deposited under different graphene concentrations. The inset in (b) shows corresponding Tafel plots.

**Table 3.** Kinetic parameters of Ni-Fe-Co alloy and Ni-Fe-Co-graphene composite coatings deposited under different graphene concentrations.

Concentration of graphene (g L <sup>-1</sup> )	b (mV dec <sup>-1</sup> )	<i>j</i> <sub>0</sub> (μA cm <sup>-2</sup> )
–	127.7	83.8
0.05	119.5	102.5
0.1	107.6	187.9
0.2	82.5	272.3
0.4	121.1	146.6
0.8	124.8	91.3

**Table 4.** Comparison of HER performance for Ni-Fe-Co-graphene composite coating with reported electrocatalysts.

Catalysts	Electrolyte solution	$\eta_{10}$ (mV)	Reference
Ni-Fe-Co-graphene	6 M KOH	169	This work
Ni-S-Fe	30 wt% KOH	222	[33]
Ni-rGO	1 M KOH	330	[34]
NiFe LDH/NF	1 M KOH	210	[37]
MoS <sub>2</sub> /Mo	1 M KOH	184	[38]
Ni <sub>3</sub> S <sub>2</sub> /nickel foam	1 M KOH	223	[39]

EIS studies. Fig. 4a shows the fitted Nyquist plots of the Ni-Fe-Co alloy and Ni-Fe-Co-graphene composite coatings in a 6 M KOH solution. The high-frequency (HF) region corresponds to the charge transfer process, and the low-frequency (LF) region corresponds to the hydrogen adsorption process [40]. As shown in Fig. 4a, EIS response is characterized by one short linear segment with an angle of approximately  $45^\circ$  and one deformed semicircle in the complex plane plot for all coatings, which indicated that HER was related to the kinetics and diffusion [41, 42]. Furthermore, the LF regions connected with the adsorption relaxation apparently disappear, and only the HF regions connected with the charge transfer remain observable. This condition was caused by the promotion of the adsorption process and the domination of the impedance response by the charge transfer process [43]. Hence, HER was controlled by the Heyrovsky reaction [44-46]. The coating under the graphene concentration of  $0.2 \text{ g L}^{-1}$  presented a smaller arc radius than did the other coatings in Fig. 4a, implying that it had a smaller resistance and overpotential for HER. Generally, the HER pathway could be via the Volmer–Tafel process or the Volmer–Heyrovsky process in an alkaline solution. The following are the HER reactions [47-49]:



where  $M$  represents a metal atom and  $H_{ads}$  denotes an H atom adsorbed at an active site of the coating. The element equivalent circuit (EEC) fitted with the EIS data by software (ZSimpWin) is shown in Fig. 4b, where  $R_s$  is the electrolyte resistance,  $R_{ct}$  is the charge transfer resistance,  $R_p$  is the resistance associated with the hydrogen adsorption,  $CPE_1$  is the constant phase element, and  $C_p$  is the double-layer capacitance of the coating surface. The corresponding EEC parameters obtained from the impedance measurements are shown in Table 5. The calculated  $R_{ct}$  of the composite coating under the graphene concentration of  $0.2 \text{ g L}^{-1}$  was the smallest ( $15.73 \text{ } \Omega \text{ cm}^{-2}$ ) among those of all coatings. The decreased transport resistance indicated a faster charge transfer process or a faster HER rate compared with that of the other coatings. The electrochemical surface area (ECSA) is a key parameter for an advanced electrode and can be obtained by the average double-layer capacitance  $C_{dl}$  (eq. 3) [50].

$$C_{dl} = \left[ \frac{Q_1}{(R_s^{-1} + R_{ct}^{-1})^{1-n_1}} \right]^{\frac{1}{n_1}} \quad (3)$$

Given the value of  $20 \text{ } \mu\text{F cm}^{-2}$  used in the literature [40], the ECSA of the coatings were obtained by division of the  $C_{dl}$  value. The coating under the graphene concentration of  $0.2 \text{ g L}^{-1}$  exhibited a much larger ECSA ( $686.5 \text{ cm}^2$ ) than did the other coatings. This finding was consistent with the analysis results of SEM.

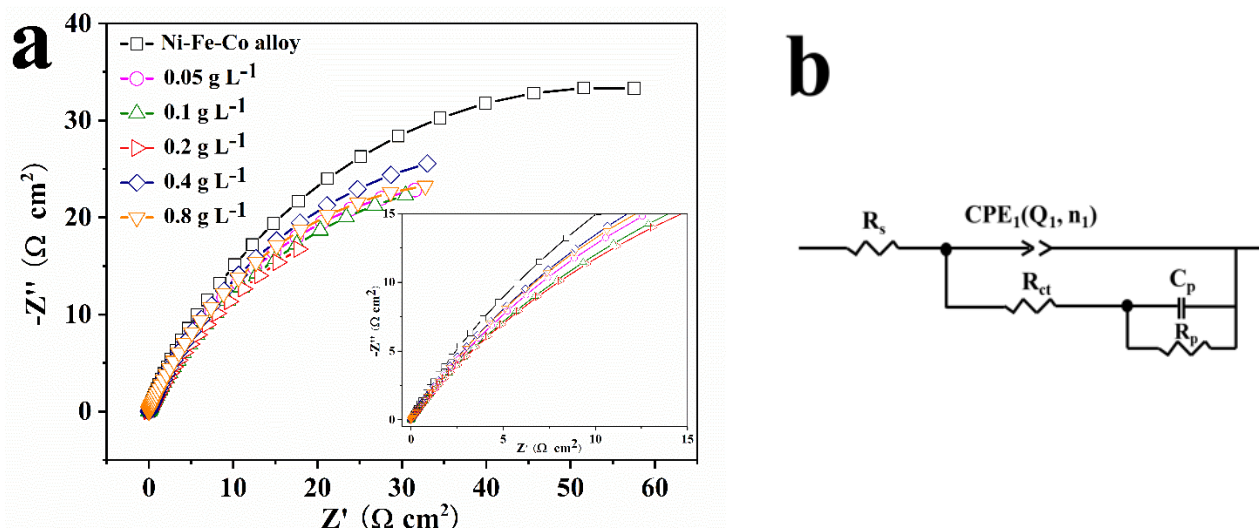


**Figure 4.** (a) Fitted Nyquist plots and (b) EEC of Ni-Fe-Co alloy and Ni-Fe-Co-graphene composite coatings deposited under different graphene concentrations.

**Table 5.** EEC parameters of Ni-Fe-Co alloy and Ni-Fe-Co-graphene composite coatings deposited under different graphene concentrations.

Concentration of graphene (g L <sup>-1</sup> )	R <sub>s</sub> (Ω cm <sup>-2</sup> )	Q <sub>1</sub> (Ω <sup>-1</sup> cm <sup>-2</sup> s <sup>-1</sup> )	n <sub>1</sub>	R <sub>ct</sub> (Ω cm <sup>-2</sup> )	R <sub>p</sub> (Ω cm <sup>-2</sup> )	C <sub>dl</sub> (μF cm <sup>-2</sup> )	ECSA (cm <sup>2</sup> )
-	0.60	4.70×10 <sup>-3</sup>	0.80	68.66	14547	1027.6	51.4
0.05	0.52	9.72×10 <sup>-3</sup>	0.83	58.04	9906	4434.5	221.7
0.1	0.56	1.55×10 <sup>-2</sup>	0.87	51.83	9551	9937.1	496.8
0.2	0.52	2.17×10 <sup>-2</sup>	0.86	15.73	7573	13730.9	686.5
0.4	0.58	9.48×10 <sup>-3</sup>	0.88	48.73	8559	8599.6	429.9
0.8	0.58	8.99×10 <sup>-3</sup>	0.86	63.99	9574	7782.4	389.1

Activation energy studies. The apparent energy of activation is also an important kinetic parameter in analyzing the electrocatalytic activity for catalysts. In this study, the LSV curves of the Ni-Fe-Co-graphene composite coating under the graphene concentration of 0.2 g L<sup>-1</sup> was investigated from absolute temperature 298 K to 328 K. As shown in Fig. 5a, with the temperature increase, the onset potential shifted toward the positive direction. This observation indicated that the overpotential was reduced, thereby leading to obtaining the same rate of chemical reactions for HER. An Arrhenius plot was obtained according to the following Arrhenius equation (eq. 4) [43]:

$$\lg j_o = \lg A - \frac{E_a}{2.303RT} \left( \frac{1}{T} \right) \tag{4}$$

where  $j_o$  is the exchange current density,  $A$  is the pre-exponential factor,  $E_a$  is the activation energy,  $R$  is the gas constant (the value of 8.3144 J mol<sup>-1</sup> K<sup>-1</sup>), and  $T$  is the absolute temperature. The pre-exponential factor  $A$  is a constant of proportionality that considers several factors, such as the frequency of collision between and the orientation of the reacting particles. The Arrhenius plot is presented in Fig. 5b. The value calculated for the composite coating was approximately 18.3 kJ mol<sup>-1</sup>,

which was lower than that of the Ni-S-Co alloy (25.2 kJ mol<sup>-1</sup>) [51] and the Ni-Fe-Zn (62 kJ mol<sup>-1</sup>) [52]. This result further verified that HER occurred easily on the Ni-Fe-Co-graphene composite electrode due to the introduction of graphene.

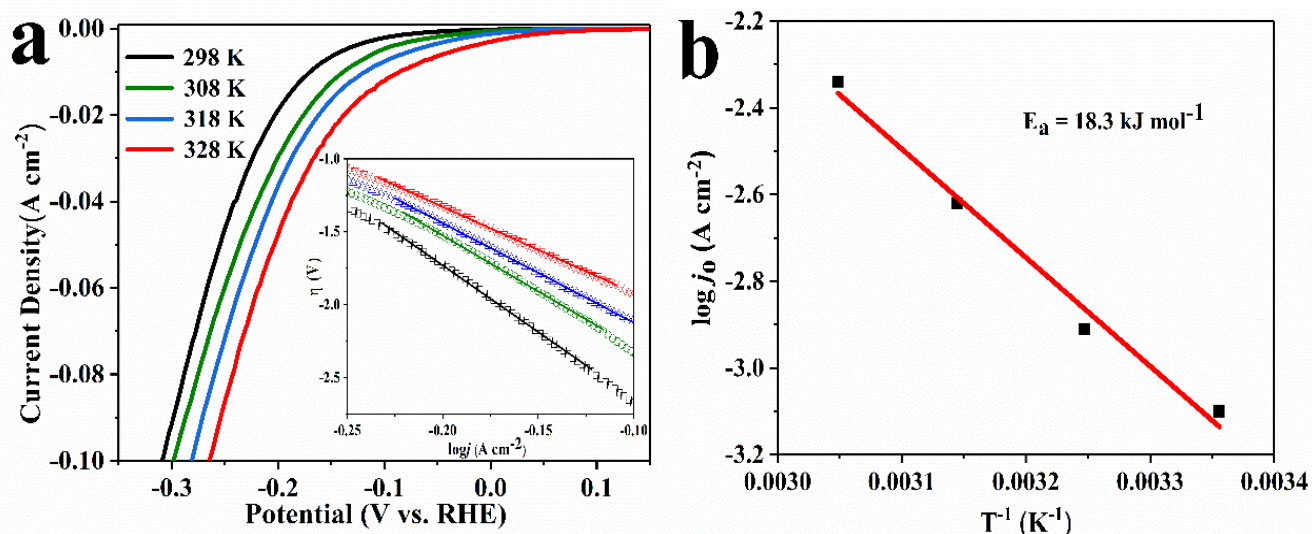


**Figure 5.** (a) LSV curves and (b) Arrhenius plot of Ni-Fe-Co-graphene composite coating at different temperatures. The inset in (a) depicts is corresponding Tafel plots.

#### 4. CONCLUSIONS

A highly electrocatalytic Ni-Fe-Co-graphene composite coating for HER was successfully fabricated by deposition in an acid sulfate bath with graphene of different concentrations. As indicated by SEM images and EIS studies, the addition of graphene could expand the electroactive surface area, which enhanced the electrocatalytic activity of the composite coating. Moreover, the largest ECSA (686.5 cm<sup>2</sup>) of the Ni-Fe-Co-graphene composite coating was approximately one order of magnitude bigger than that of the Ni-Fe-Co alloy. XRD patterns illustrated that the introduction of graphene could efficiently decrease the grain size. Meanwhile, the cathodic LSV curves and corresponding Tafel curves confirmed that the composite coating showed a minimum overpotential of HER (169 mV at 10 mA cm<sup>-2</sup>). The Tafel slope and EIS analyses showed that the HER followed the Volmer–Heyrovsky mechanism. In addition, the low apparent activation energy of the Ni-Fe-Co-graphene composite coating (18.3 kJ mol<sup>-1</sup>) was calculated and confirmed the improved electrocatalytic activity of the coating.

#### ACKNOWLEDGEMENTS

This work was financially supported by the China Scholarship Council (CSC), and Guangxi Key Laboratory of Information Materials (Guilin University of Electronic Technology), P.R. China (Project No. 171009-K).

**Reference**

1. A. Steinfeld, *Int. J. Hydrogen Energy*, 27 (2002) 611.
2. J. O. M. Bockris, T. N. Veziroglu, *Int. J. Hydrogen Energy*, 32 (2007) 1605.
3. K. Zeng, D. Zhang, *Prog. Energ. Combust.*, 36 (2010) 307.
4. A. Han, S. Jin, H. Chen, H. Ji, Z. Sun, P. Du, *J. Mate. Chem. A*, 3 (2015) 1941.
5. H. Vrabel, D. Merki, X. Hu, *Energy Environ. Sci.*, 5 (2012) 6136.
6. D. Voiry, H. Yamaguchi, J. Li, R. Silva, D. C. B. Alves, T. Fujita, M. Chen, T. Asefa, V. B. Shenoy, G. Eda, M. Chhowalla, *Nat. Mater.*, 12 (2013) 850.
7. M. A. Domínguez Crespo, A. M. Torres Huerta, B. Brachetti Sibaja, A. Flores Vela, *Int. J. Hydrogen Energy*, 36 (2011) 135.
8. F. Safizadeh, E. Ghali, G. Houlachi, *Int. J. Hydrogen Energy*, 40 (2015) 256.
9. J. M. Jakšić, M. V. Vojnović, N. V. Krstajić, *Electrochim. Acta*, 45 (2000) 4151.
10. K. Fominykh, P. Chernev, I. Zaharieva, J. Sicklinger, G. Stefanic, M. Doblínger, A. Malier, A. Pokharel, S. BoCklein, C. Scheu, *ACS Nano*, 9 (2015) 5180.
11. M. Kuang, P. Han, Q. Wang, J. Li, G. Zheng, *Adv. Funct. Mater.*, 26 (2016) 8555.
12. D. L. Stojić, Š. S. Miljanić, M. M. Jakšić, *J. New Mat. Electrochem. Syst.*, 6 (2003) 55.
13. M. Y. Gao, C. Yang, Q. B. Zhang, Y. W. Yu, Y. X. Hua, Y. Li, P. Dong, *Electrochim. Acta*, 215 (2016) 609.
14. Y. Ullal, A. C. Hegde, *Int. J. Hydrogen Energy*, 39 (2014) 10485.
15. W. Li, D. Xiong, X. Gao, W. G. Song, F. Xia, L. Liu, *Catal. Today*, 287 (2016) 122.
16. W. Li, X. Gao, X. Wang, D. Xiong, P. P. Huang, W. G. Song, X. Bao, L. Liu, *J. Power Sources*, 330 (2016) 156.
17. A. K. Geim, K. S. Novoselov, *Nat. Mater.*, 6 (2007) 183.
18. B. Łosiewicz, A. Budniok, E. Rówiński, E. Łągiewka, A. Lasia, *J. Appl. Electrochem.*, 34 (2004) 507.
19. N. A. M. Barakat, M. Motlak, B. S. Kim, A. G. El Deen, S. S. Al Deyab, A. M. Hamza, *J. Mol Catal A Chem*, 394 (2014) 177.
20. A. Arvinte, F. Doroftei, M. Pinteala, *J. Appl. Electrochem.*, 46 (2016) 1.
21. J. Yu, Y. Zhong, W. Zhou, Z. Shao, *J. Power Sources*, 338 (2017) 26.
22. S. Vadukumpully, J. Paul, N. Mahanta, S. Valiyaveetil, *Carbon*, 49 (2011) 198.
23. J. Deng, P. Ren, D. Deng, X. Bao, *Angew. Chem.*, 127 (2015) 2128.
24. S. Badrayyana, D. K. Bhat, S. Shenoy, Y. Ullal, A. C. Hegde, *Int. J. Hydrogen Energy*, 40 (2015) 10453.
25. B. Subramanya, Y. Ullal, S. U. Shenoy, D. K. Bhat, A. C. Hegde, *RSC Adv.*, 5 (2015) 47398.
26. N. Li, L. Zhang, Y. Zhu, M. Xu, Y. Xu, X. Ruan, H. Ma, *J. Electrochem. Soc.*, 165 (2018) D215.
27. Y. Liang, Y. Li, H. Wang, J. Zhou, J. Wang, T. Regier, H. Dai, *Nat. Mater.*, 10 (2011) 780.
28. C. W. Su, E. L. Wang, Y. B. Zhang, F. J. He, *J. Alloy Compd.*, 474 (2009) 190.
29. V. Torabinejad, M. Aliofkhaezai, A. S. Rouhaghdam, M. H. Allahyarzadeh, *Tribol. Int.*, 106 (2017) 34.
30. Y. K. Yoo, Q. Xue, Y. S. Chu, S. Xu, U. Hangen, H. C. Lee, W. Stein, X. D. Xiang, *Intermetallics.*, 14 (2006) 241.
31. B. E. Warren, *X-Ray Diffraction*, Dover Publications Inc., (1990), New York, USA.
32. H. Ren, W. Xu, S. Zhu, Z. Cui, X. Yang, A. Inoue, *Electrochim. Acta*, 190 (2016) 221.
33. Y. Wu, H. He, *Int. J. Hydrogen Energy*, 43 (2018) 1989.
34. L. Wang, Y. Li, X. Yin, Y. Wang, L. Lu, A. Song, M. Xia, Z. Li, X. Qin, G. Shao, *Int. J. Hydrogen Energy*, 42 (2017) 22655.
35. Y. Cao, H. Liu, X. Bo, F. Wang, *Sci. China. Chem.*, 58 (2015) 501.
36. Z.X. Cai, X.H. Song, Y.R. Wang, X. Chen, *ChemElectroChem*, 2 (2015) 1665.
37. J. Luo, J. H. Im, M. T. Mayer, M. Schreier, M. K. Nazeeruddin, N. G. Park, S. D. Tilley, H. J. Fan,

- M. Grätzel, *Science*, 345 (2014) 1593.
38. Z. Pu, Q. Liu, P. Jiang, A. M. Asiri, A. Y. Obaid, X. Sun, *Chem. Mater.*, 26 (2014) 4326.
  39. L. L. Feng, G. Yu, Y. Wu, G. D. Li, H. Li, Y. Sun, T. Asefa, W. Chen, X. Zou, *J. Am. Chem. Soc.*, 137 (2015) 14023.
  40. D. A. Harrington, B. E. Conway, *Electrochim. Acta*, 32 (1987) 1703.
  41. J. P. Diard, B. L. Gorrec, C. Montella, *J. Electroanal. Chem.*, 471 (1999) 126.
  42. L. Birry, A. Lasia, *J. Appl. Electrochem.*, 34 (2004) 735.
  43. I. Herraiz Cardona, C. González Buch, C. Valero Vidal, E. Ortega, V. Pérez Herranz, *J. Power Sources*, 240 (2013) 698.
  44. L. Bai, D. A. Harrington, B. E. Conway, *Electrochim. Acta*, 32 (1987).
  45. B. E. Conway, R. E. White, I. Ebrary, *Modern aspects of electrochemistry*, Springer, (2009), New York, USA.
  46. N. A. Assunçao, M. J. Giz, G. T. Filho, E. R. Gonzalez, *J. Electrochem. Soc.*, 144 (1997) 2794.
  47. R. Baba, S. Nakabayashi, A. Fujishima, *K. Honda, J. Phys. Chem*, 89 (1985) 1902.
  48. L. Mihailov, T. Spassov, M. Bojinov, *Int. J. Hydrogen Energy*, 14 (2012) 10499.
  49. X. Yu, M. Wang, Z. Wang, X. Gong, Z. Guo, *Electrochim. Acta*, 211 (2016) 900.
  50. G. J. Brug, A. L. G. van den Eeden, M. Sluyters Rehbach, J. H. Sluyters, *J. Electroanal. Chem. Interf. Electrochem.*, 176 (1984) 275.
  51. Q. Han, K. Liu, J. Chen, X. Wei, *Int. J. Hydrogen Energy*, 28 (2003) 1345.
  52. M. J. Giz, S. C. Bento, E. R. Gonzalez, *Int. J. Hydrogen Energy*, 25 (2000) 621.

© 2019 The Authors. Published by ESG ([www.electrochemsci.org](http://www.electrochemsci.org)). This article is an open access article distributed under the terms and conditions of the Creative Commons Attribution license (<http://creativecommons.org/licenses/by/4.0/>).